The Characterization of Cannabidiol Amorphous Solid Dispersions

by

Brandon Blass

A Thesis Presented in Partial Fulfillment
of the Requirements for the Degree
Master of Science

Approved March 2019 by the
Graduate Supervisory Committee:

Jeff Yarger, Chair
Greg Holland
Gary Moore

ARIZONA STATE UNIVERSITY

MAY 2019

ABSTRACT

Generating amorphous solid dispersions (ASDs) containing active pharmaceutical ingredients has become a favorable technique of emerging prominence to improve drug solubility and overall bioavailability. Cannabidiol (CBD) has now become a major focus in cannabinoid research due to its ability to serve as an anti-inflammatory agent, showing promising results in treating a wide array of debilitating diseases and pathologies. The following work provides evidence for generating homogenous glass phase amorphous solid dispersions containing 50% (w/w) up to 75% (w/w) CBD concentrations in the domain size of 2 – 5 nm. Concentrations up to 85% (w/w) CBD were concluded homogenous in the supercooled liquid phase in domain sizes of 20 – 30 nm. The results were obtained from polarized light microscopy (PLM), differential scanning calorimetry (DSC), as well as solution and solid-state NMR spectroscopy.

ACKNOWLEDGMENTS

The work documented within this thesis could not have been accomplished without the generous support provided by my research group. My start within this research group would have never come to fruition if it were not for Professor Greg Holland initially bringing me on board as an undergraduate researcher. His belief in my work ethic along with his instruction and guidance through my first attempts at research gave me not only the confidence needed to accel, but also cemented a sense of belonging in a time when I was lost. To this my gratitude extends infinitely in his direction. The opportunity provided by Professor Jeff Yarger to work within his research group as a master's student was one that altered my career path in a most positive direction. He served as an excellent role model and coached me through some of my most difficult and unorthodox challenges I faced in both my academic and professional career. To that I cannot express how thankful I am for Professor Yarger being a part of my life. I'd like to thank Dr. Stephen Davidowski as he stood by my side as an excellent mentor guiding me through the more challenging aspects of understanding the abstract subject of NMR analysis as well as kept me on track through my academic progression, and all the while elegantly strengthened the already established friendship we had stemming back over the past decade. I'd additionally like to thank Dr. Brian Cherry and Dr. Samrat Amin just as well for providing immense insight and understanding through my academic challenges, and for continuing to uphold our solid friendships that I will cherish for years to come. I'd like to thank and recognize Ashlee Williams for assisting in the execution of conducting DSC analysis, serving as an excellent colleague, and for being a great support system throughout the progression of our shared academic courses we pushed through together. I'd like to recognize and thank my wife for

believing in my capabilities as an aspiring scientist and providing the structure in my life that allowed me to achieve my life ambitions, my brother for instilling the life morals and virtues I base my way of living on, my mother for providing me the unique ability to perceive the world through an artistic lens, my grandparents for instilling discipline into my life, and lastly my father for passing on his passion and gift for understanding chemistry onto me and a never-ending desire to investigate the world through a scientific means. It was his belief that everything happens exactly the way it is supposed to. May his soul rest in peace.

TABLE OF CONTENTS

Page

LIST OF FIGURES

Figure Page

LIST OF TABLES

Table Page

Introduction

Cannabinoids and the Endocannabinoid System:

Due to the loosening of restrictions on cannabinoids in recent years, their therapeutic effects on the human body have been the focus of a large amount of recent research.[1–5] Therapeutic benefits from cannabinoids have been documented in many clinical case studies over the past decade. Treatment of many diseases and disorders such as Crohn's Disease, Parkinson's Disease, and even in pediatric cases involving cerebral palsy with cannabinoids have shown promising results.[3,4,6] However, with such a vast amount of fundamental research untouched, the need for furthering the understanding of cannabinoids and their interactions with the endocannabinoid system must be approached. Cannabinoids isolated from C. *sativa* are classified as exocannabinoids as opposed to the human body's naturally produced endocannabinoids and both play integral roles in the immune response and are attributed to inducing a wide range of molecular interaction with the human endocannabinoid system.[7,8]

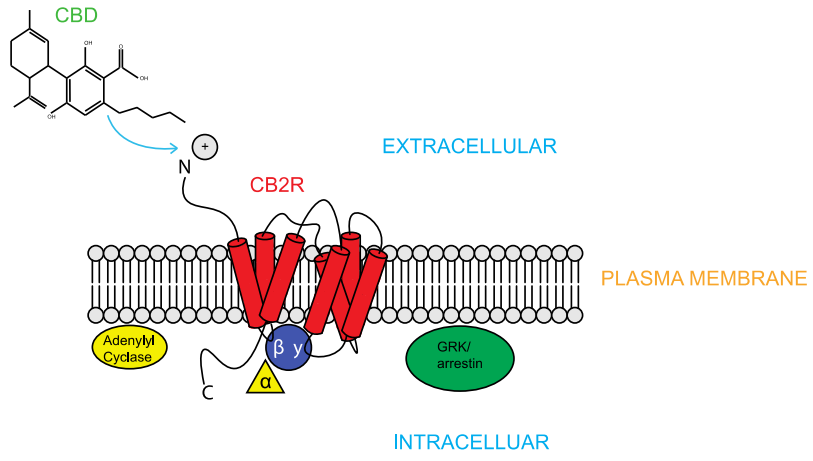

Figure 1: Schematic displaying the activation of CB2 receptor via cannabidiol. As a G coupled protein receptor, activation induces an array of cellular signaling activity.

The two main receptor types found within the endocannabinoid system are known as cannabinoid type 1 (CB1) and cannabinoid type 2 (CB2) receptors, and both of which are classified as A serpentine receptors which interact dynamically with $G_{i/o}$ proteins leading to a cascade of cell signaling activity. [8–10]

The CB2 receptor is found primarily in the peripheral nervous system (PNS) and is distinguished from its counterpart in that upon ligand binding, induces no psychoactive effects.[7,8] The non-planar molecular structure of cannabidiol (CBD) prevents ligand binding interactions from occurring between it and the CB1 receptor, and therefore CBD induces no psychoactive effects, but instead acts as an anti-inflammatory agent by binding to CB2 receptors of the PNS and immune-system.[7] The ability to induce expression of the CB2 receptor is a very high, with expression increases up to 100 fold post tissue damage and continues through the inflammatory process.[8] As it has been determined that all immune cells express CB2 receptors, reports have shown that inflammatory-mediated demyelinating pathology improvement is seen in response to CB2 immune cell activation.[7] As a reported anti-inflammatory cannabinoid that induces no psychoactive side effects, CBD presents itself as an excellent candidate for lead natural compound drug development.

Pharmacokinetics, Phase, and Bioavailability:

The pharmacokinetics of drug absorption, distribution, metabolism, and extraction (ADME) dictate oral drug therapeutic design.[11] In the case of developing an orally administered drug therapeutic, while common factors of hydrophobicity of the drug must be accounted for, the phase of active pharmaceutical ingredient (API) must be accounted for as well. The

physical state of the API can have a dramatic impact on the bioavailability, and thus the efficacy of the drug.[11,12]

Crystalline APIs are attributed with a discrete structural lattice holding a low energy state dominated by strong intermolecular forces.[13] As such, a large energy input is required to disrupt the molecular lattice of the API upon digestion.[12] Comparatively, an API in the glass phase can greatly increase dissolution and therefore enhance bioavailability properties of the API and is due to the high entropy state associated with the intermolecular forces of a glass phase API.[12]

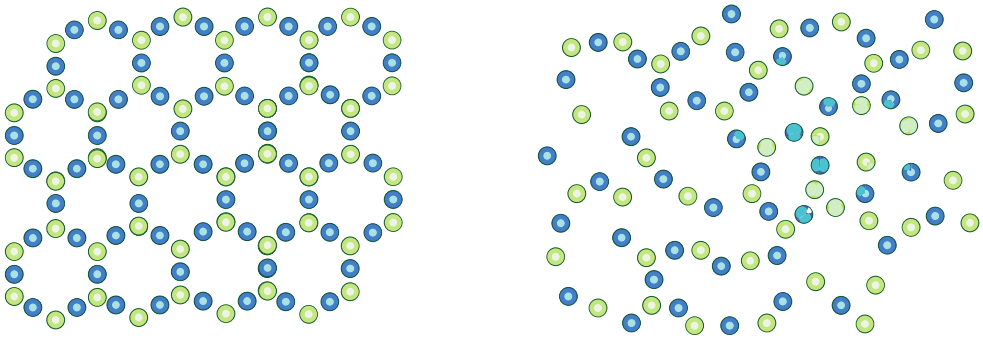

Figure 2: Depiction of a crystalline material (left) compared to an amorphous material (right). The intermolecular forces holding each molecule together shows a discrete organization in a crystalline material versus the disrupted molecular lattice of an amorphous material.

While a crystalline material has regular order in the arrangement of molecules in a lattice, amorphous (or glassy) materials lack this order. Good glass formers are molecules which resist crystallization when cooled below their melting point (T_m), allowing them to become "supercooled" liquids. If a material continues to be cooled and does not crystallize, at some point translational molecular motion will cease. The temperature at which this occurs is referred to as the glass transition (T_g) of a material.[14,15] By cooling a material very quickly

from above its melting point to below T_g the likelihood of the material crystallizing can be minimized, in a process commonly referred to as quenching.[13,14] As seen in Figure 3, a liquid material's temperature must fall below its T_m to adopt a supercooled liquid state of matter and then further drop below the T_g before it has reached a hardened glass state.[12,13] Therefore, bringing the temperature of an API past its T_m will allow for a liquid phase to be reached which in turn can be immediately quenched resulting in the formation of an ASD API.[12–14]

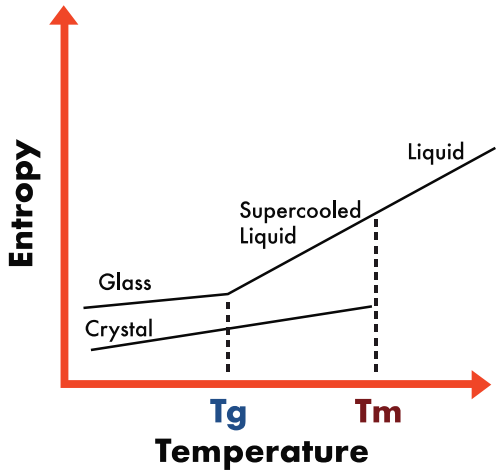

Figure 3: Phase diagram comparing the entropy associated with crystalline materials and amorphous materials as a function of temperature. The higher entropic state of amorphous materials represented by the glass, supercooled liquid, and liquid phases provide not just the phase differences between T_g and T_m but also show the rate of entropy change associated with each phase.

It is the glass phase that an API resembles the macroscopic characteristics of a solid yet holds the molecular organization of high entropy fluid states.[13,14] And while some materials may hold a stable glass phase for an extensive amount of time, other materials may recrystallize over time due to such a lower activation energy barrier associated with the API amorphous state.[12] The lowest energy state associated with matter is observed in the crystal phase and thus there is the natural drive to reach this stability when materials are in higher energy phases.[13] This presents a challenge in the pharmaceutical industry when

designing an amorphous oral therapeutic, as shelf life becomes an obstacle.[12,14] In order to achieve the beneficial properties of bioavailability from an ASD, APIs are commonly mixed with polymers which help to increase glass phase stability.[12]

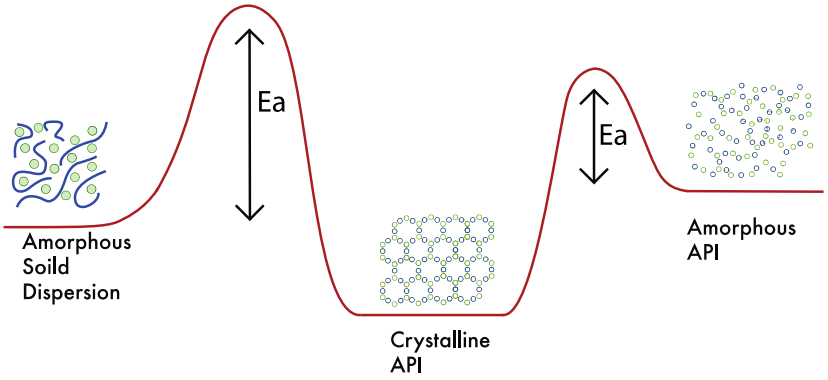

Figure 4: Energy diagram depicting energy barriers that must be overcome in order to transition from an amorphous state into a crystalline state for an API. A pure API in the amorphous state will be attributed with a smaller energy barrier when transitioning into the crystal phase. Addition of a polymer into a binary mixture containing the API greatly increases the needed energy input required induce phase transition into a crystalline state.

In the case where an API alone holds a T_g below room temperature, recrystallization becomes an issue in oral therapeutic design. In order to raise the T_g above room temperature, and increase the stability of the amorphous solid dispersion, a polymer must be selected with a high enough of a T_g that allows for glass stability above room temperature of the mixture, yet low enough such that the T_g of the mixture is reasonably attainable.[12] With a proper combination of polymer and API, the antiplasticizing effect brought about by the polymer will result in molecular mobility reduction and a retardation in the crystallization process therein.[12]

Increasing the T_g of an API can be achieved by incorporating the addition of a polymer. However, the intimate mixing at the molecular level of both components must is critical. Inadequate mixing of the components would inevitably lead to phase separation, API recrystallization, and therefore defeat the purpose of incorporating a polymer when designing an ASD oral therapeutic.[12,16] In the context of oral therapeutics, the miscibility of an ASD binary mixture refers to the degree of homogeneity an API and chosen polymer display when both components are mixed.[12,16,17] Figure 5 depicts the difference in levels of miscibility between an API and polymer.

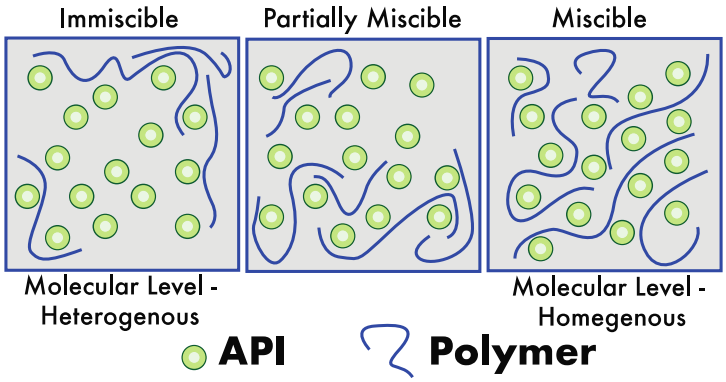

Figure 5: Three levels of miscibility between an API and a polymer where the API domain is considered densely packed in an immiscible state, partially miscible with an increase in saturation of API with polymer, and a supersaturated state where the API and polymer are miscible and therefore intimately mixed at the molecular level.

Production and Characterization of ASD Oral Therapeutics:

The technological advancement in ASD oral therapeutic development has progressed over the years with the development of hot melt extrusion and spray drying techniques holding a predominant method in pharmaceutical designs.[1618] Other methods of rendering APIs and polymers into a miscible state include ball milling and even classical grinding via mortar and pestle.[16] Regardless of the chosen method in designing an ASD oral therapeutic,

analytical methods for evaluating the miscibility of ASD systems have just as well advanced through the years. Some of the most common techniques utilized to evaluate ASD miscibility in a binary mixture include X-ray diffraction (XRD), differential scanning calorimetry (DSC), Raman spectroscopy, infrared (IR) spectroscopy, and solid-state nuclear magnetic resonance (SSNMR) spectroscopy.[12,13,16,18] While the above analytical methods can be considered relatively extensive, providing vast amounts of information when investigating thermodynamic properties and/or the physical states of matter, more simplistic approaches such as polarized light microscopy (PLM) can provide a qualitative assessment of phase determination at a relatively low cost.[18]

A miscible system can be characterized by a single T_g where the individual glass transition points intrinsic to either API or polymer are no longer detectable but rather both components display an intermediate T_g.[19,20] DSC provides the capability of detecting the T_g of amorphous solid dispersions allowing for homogeneity of a binary mixture to be evaluated.[16,19,20] Still it has been documented that a homogenous mixture can still display two glass transition points and additionally, a phase separated ASD can hold an intermediate T_g.[19–21] While DSC is a technique useful in evaluating miscibility of an ASD, domain size limitations of miscibility are limited to a range of ~20 – 30 nm.[16,22] However, SSNMR however provides a means of detecting homogeneity of an ASD in the domain of 2-5 nm, and therefore provides even greater insight into how well an ASD is mixed at the molecular level.[16] A limitation of SSNMR is that attempting magic angle spinning on a material characterized as a "super cooled" liquid could potentially lead to detrimental probe damage upon analysis without proper equipment.[23] A combination there within of multiple

techniques is advantageous when evaluating the properties and characteristics of ASD systems.

Analytical Techniques:

Polarized light microscopy is a technique which involves the manipulation of white light normally produced by a regular microscope in the process of viewing a specimen or sample at higher magnification. While white light vibrates randomly in all directions, polarized light waves vibrate unidirectionally.[22] This is achieved by passing the white light produced by the microscope through a polarized filter aligned in an east west direction prior to passing through the sample.[22] The directional limitation of light wave vibrations allow for the detection of a phenomenon known as birefringence, or the double-refraction of light, through an anisotropic material. Birefringence is detected as it passes through anisotropic materials into a secondary polarized filter termed an analyzer.[22] A substance that is anisotropic can be characterized as a material having directional dependence in its lattice organization.[22] A great example of an anisotropic material would be a crystal. The structural lattice of a crystal is directionally dependent and the incident light that passes through refracts at two distinct angles. As the crystal is rotated clockwise or counterclockwise perpendicular to the polarized incident light, birefringence can be observed in the form of distinct color changes as the wavelengths of refracted light are altered passing through the anisotropic lattice and then into the analyzer.[17,22] This in turn provides an easy means of performing a qualitative analysis for phase determination with respect to amorphous solid dispersions.[17,22]

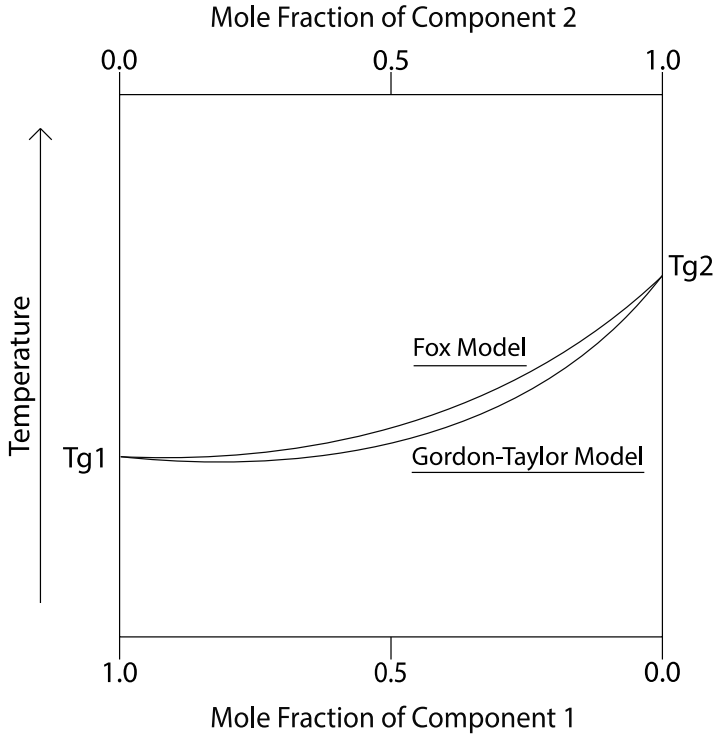

Figure 6: Diagram depicting the two types of T_g change of a homogenous binary mixture composed at various compositions. The bottom curve represents the theoretical change in T_g based on the Gordon-Taylor model, while the top curve represents the theoretical change in T_g based on the Fox-model. As component 1 decreases in composition while component 2 increases in composition, the T_g of component 1 begins to increase and vice versa for its counterpart.

Differential scanning calorimetry is a thermoanalytical technique providing a means to measure the quantity of heat required to increase the sample temperature compared to that of a reference.[15,24] The resulting thermogram plots heat flow measured in W/g as a function of temperature, and thus phase changes of the sample can be accurately determined. If a series of ASD binary mixtures varying in percent composition are analyzed, shifts in phase transition temperatures for each amorphous material become apparent. By evaluating the T_g of ASD binary mixtures varying in percent composition, the defined T_g pertaining to each mixture can then be plotted against wt% composition of either component.[15] When ASD binary compositions are intimately mixed at the molecular level and thus considered homogenous, the experimental intermediate T_g of each composition should be comparable

to the calculated T_g's acquired from the Fox model and/or the Gordon-Taylor model.[15,25,26] The Gordon-Taylor model, equation 1, calculates the intermediated T_g of an ASD binary composition based on weight fractions of component one x_1, the glass transition temperatures of each pure component T_{gi}, and a fitting parameter $k_{G\text{-}T}$, acquired from the quotient of the products of density and change in thermal expansion (CTE) coefficients respective of each component.[25,26] CTE represents each components' isobaric expansivity differences in the process from transitioning from a liquid to a glass phase.[25]

$$T_g = \frac{(1\text{-}x)T_{g1} + k_{G\text{-}T}xT_{g2}}{(1\text{-}x) + k_{G\text{-}T}x} \quad (1)$$

$$k_{G\text{-}T} = \frac{\rho_1 \Delta\alpha_1}{\rho_2 \Delta\alpha_2} \quad (2)$$

$$k_{G\text{-}T} = \frac{\rho_1 T_{g1}}{\rho_2 T_{g2}} \quad (3)$$

The Simha-Boyer equation is utilized to simplify the Gordon-Taylor model allowing the elimination of factoring in the thermal expansion coefficient to derive the value of $k_{G\text{-}T}$.[25–28] The Simha-Boyer rule states that the CTE of a liquid polymer will always be larger than its glass state CTE, and thus the approximation of $\rho\Delta\alpha$ at $T_g = 0.133$ can be applied.[25,26] The Simha-Boyer rule dictates that k can be approximated to equation 3 above.[25–28] As the value of the parameter $k_{G\text{-}T}$ increases, the predicted intermediate T_g for each binary mixture increases by a factor of $k_{G\text{-}T}$'s value with wt% polymer increase. Further simplification of the Gordon-Taylor model is applicable when densities of both components are approximately the same, however a slightly less accurate T_g predication results.[27,28] This simplification removes the parameter $k = 1$ in the Gordon-Taylor model, and the resulting

equation is termed the Fox model.[27,28] The Fox model, equation 5, provides the reciprocal intermediate T_g based on weight percent and pure component T_g alone, assuming $k = 1$.[27,28]

$$\frac{1}{T_g} = \frac{x_1}{T_{g1}} + \frac{x_2}{T_{g2}} \tag{4}$$

A basic representation of each model can be seen in Figure 6 where the top curve is representative of the Fox-model, and the bottom representative of the Gordon-Taylor-model. In the past couple decades however, another variation on the Gordon-Taylor model was introduced by Kwei *et al*. to which an additional fitting parameter was introduced into the Gordon-Taylor equation.[25,26] Equation 5 shows this rendition to the Gordon-Taylor model and is known as the Kwei model, where, x is the wt% fraction of component 2, and q is an additional fitting parameter that considers the effects from component interactions such as hydrogen bonding, ion-dipole forces, and Van der Waals interactions on stabilization.

$$T_g = \frac{(1-x)T_{g1} + k_{G\text{-}T}xT_{g2}}{(1-x) + k_{G\text{-}T}x} + q(1-x)(x) \tag{5}$$

Kwei proposed that in a binary system of two polymers, evaluating the excess energy related to the polymer backbone stabilization in the binary system allows for comparison to that of the weighted average of each polymer backbone stabilization within separate systems.[26] If the required average thermal energy needed to breach the energy barriers rendering polymer backbones immobile below T_g is measured as the product of the $\kappa_B T_g$, then the product $\kappa_B q x_1 x_2$ is the excess energy related to polymer backbone stabilization in a binary system.[26] The term κ_B is the Boltzmann constant, and T_g is the intermediate glass transition temperature of the binary system.[26] The energy barriers associated with polymer

backbone immobilization at the T_g include intramolecular flex energy as well as intermolecular hole energy.[26] These interactions are represented in Figure 7 as pairs of contact, where in the case of an API and a polymer blend, three types of interactions can occur.[26]

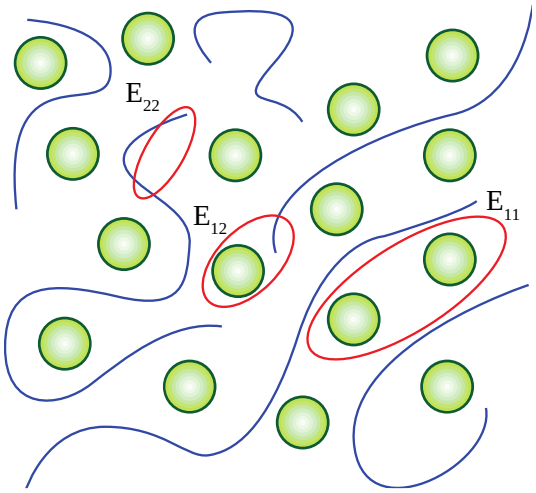

Figure 7: Lattice model of a binary mixture composed of API and polymer. The three types of interactions that can occur include homocontacts between polymer units, homocontacts between API units, and heterocontacts between API and polymer. The contribution from each interaction inducing stabilization is denoted by E_{ii}, where E_{11} are the interactions between API and API, E_{22} are the interactions between polymer unit and polymer unit, and E_{12} is the interaction between API and polymer unit.

When incorporating the volume fractions (Φ_{ii}), of each contact type with respective backbone stabilization contributions (E_{ii}), the excess backbone stabilization energy of the polymer mixed with API over the weighted mean backbone stabilization energy of the polymer and weighted mean stabilization of the API alone can be expressed through Equation 6.[26]

$$\kappa_B q x_1 x_2 = \emptyset_{12} E_{12} + \emptyset_{11} E_{11} + \emptyset_{22} E_{22} - 0.5(E_{11} + E_{22}) \quad (6)$$

The probability of finding a hetercontact Φ_{12} in any location of the lattice is dependent upon the binary mixture composition.[26] Only contacts resulting from neighboring units of immediate proximity are considered and for simplification only 6 contacts are accounted

for.[26] Of the 6 contacts, two of which will always be homocontacts between two units of the polymer.[26] Therefore, the contact type resulting from the remaining four will occur as statistical distribution of homo and heterocontacts proportional to the wt% of each component.[26] Hence, the probability of heterocontact formation within the binary mixture is $(4/6)x_1x_2$.[26] When the case of an API and polymer are the components of the binary system intimately mixed at the molecular level, random distribution of each component is assumed ideal.[16,26] The intermediate T_g predictions based of the Kwei model dictate when ($q > 0$) high intermediate T_g's can be expected to result due to higher excess energies, and when ($q < 0$), smaller intermediate T_g's are to be expected due to lower excess energies.[26] It is this extra fitting parameter that accounts for the intermolecular forces between components allowing for a more accurate T_g prediction.[25,26]

SSNMR is a powerful analytical technique utilized to investigate solid materials much like in solution state NMR, but SSNMR must take advantage of a phenomenon known as magic-angle spinning (MAS) to acquire useful information.[29,30] The intrinsic spins associated with the nuclei composing the sample experience several interactions causing broad signals to arise upon Fourier-transformation (FT) of the free induction decay (FID).[29,30] However, by spinning the sample at the magic angle (~54.74˚) with respect to the applied static magnetic field (B_o), interactions responsible for the broadening of signals such as dipole-dipole interactions, chemical shift anisotropy (CSA) interactions, and quadrupolar interactions can be averaged out, improving the resulting signals in the FT spectrum.[29,30] Cross polarization (CP) is also a useful technique employed when probing solid samples and is commonly used in conjunction with MAS, and when both techniques

are combined, they are termed cross polarization magic-angle spinning (CPMAS).[16,29,30] Cross polarization is a signal to noise (s/n) enhancing technique where in the polarization from abundant spins such as ^{1}H nuclei are transferred over to far more dilute spins from isotopes such as ^{13}C.[30] Additionally, the extended time taken for slow relaxation of dilute isotopes to return back into the static field can be circumvented as the recycle delay is based on the spin lattice relaxation of the abundant nuclei. Proton decoupling after CP, further optimizes the s/n in the resulting FT spectrum.[16,29,30] A combination of the above techniques allows for SSNMR investigation into the miscibility of a ASD binary mixtures and the molecular dynamics of both components.[16,30]

Two basic types of SSNMR experimental approaches can be employed to investigate the miscibility of a sample composed of an ASD. Spin lattice relaxation (T_1) and spin-lock relaxation ($T_{1\rho}$) experiments allow for evaluation of relaxation rates in two different time domains.[16,17,30] Spin-lattice relaxation refers measuring the time taken for radio frequency (RF) irradiated nuclei to relax back into the applied static field following a π pulse.[30,31] In this case, a pulse sequence can be applied to the sample nuclei such that the bulk magnetization associated with the sample is tipped 180˚ with respect to the B_o field. The bulk magnetization immediately begins to relax as it precesses back towards the B_o field. After a specified delay time (τ) has occurred, a RF $\pi/2$ pulse irradiates the nuclei again. This pulse pattern is applied over a series of delay time increments and a logarithmic pattern is observed in signal intensity upon arraying the resulting FT spectra acquired from each free induction decay (FID).[30,31] This type of measurement is referred to as an inversion recovery experiment.[16,30,31] Spin-lock relaxation refers to pulsing nuclei 90˚ with respect

to the B_o field and then locking their magnetization along the transverse axis by a secondary RF field.[30,32] The decay rates of transverse magnetization from each component can then be measured.[30]

In both types of relaxation, spin diffusion, or the process of mutual magnetization exchange occurring from polarized spins in different localized sites coming to equilibrium with respect to the B_1 locked magnetic field, can be used to access internuclear distances.[16,33] Intimate molecular mixing of two components in an ASD is successful when the proximity of each component is closer than that of the length scale of spin diffusion.[16,33] Slow relaxing components transfer magnetization to faster relaxing components and the weighted average of these values from each component is equal to the relaxation time for both as a whole.[16,29] The following equation describes the length scale of spin diffusion.[16]

$$L^2 = 6Dt \tag{8}$$

Where D represents the spin diffusion coefficient equal to 10^{-12} cm^2/s,[16] and t represents the rate of relaxation time.[16,33] The length scale for spin diffusion of 20 – 50 nm ranges between 1 to 5 s for spin lattice relaxation times while the length scale for spin diffusion of 2 – 5 nm ranges between 5 and 50 ms for spin-lock relaxation times.[16,29] If domain size of homogeneity is shorter than 2 – 5 nm, T_1 and $T_{1\rho}$ times from each component will be comparable. If homogeneity occurs within the domain size of 5 – 20 nm, then a comparable T_1 time will be observed from each component yet the $T_{1\rho}$ time for each component will differ. And finally, if homogeneity is achieved in the range of 20 – 50 nm or greater, both relaxation times will vary for each component.[16,29]

Experimental

Material Preparation:

Polyvinylpyrrolidone (PVP) with an average molecular weight of ~29,000 g/mol and was procured from Sigma Aldrich. The PVP was vacuum dried over night at 70˚C. The cannabidiol (CBD) isolate was purchased from Standard Hemp Company (Denver, CO) and both components were stored seperately in 20mL scintillating vials and placed under drierite at all times unless utilized. Below is an image depicting the molecular structure of the two components.

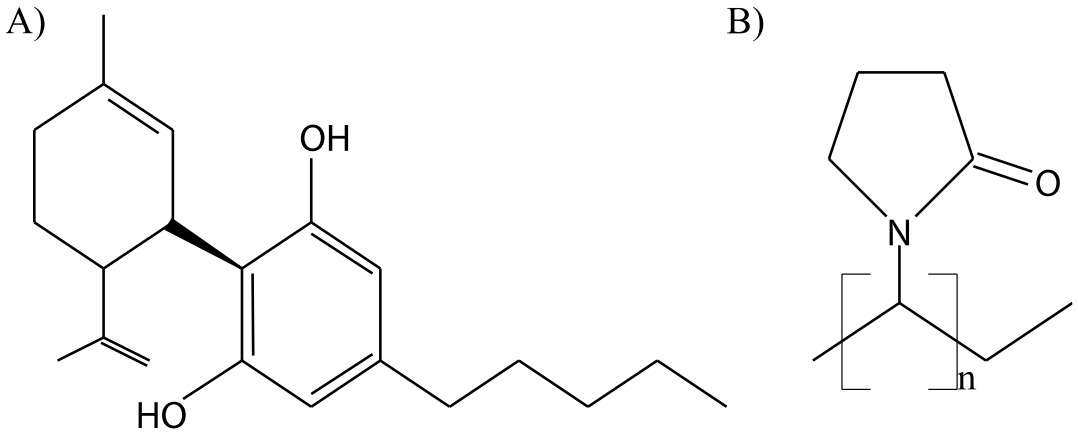

Figure 8: Molecular representation of A) cannabidiol (CBD) and B) polyvinylpyrrolidone (PVP) monomer. The backbone of the PVP polymer is denoted by n, indicating the number of repeating.

Synthesis:

Physical mixtures of the API and polymer were created by wt% and combined together in a 100 mm I.D. agate mortar and ground with an agate pestle. A total of six samples with masses of 80 mg were generated with the following CBD wt% composiitons: 0%, 50%, 55%, 65%, 75%, and 85%. Physical mixing occurred by grinding the mixtures three times for five minutes with stirring for two minutes between each grinding. The stirring of each

mixture was executed in the mortar with the edge of a 3x3 inch VWR weigh paper folded in half ensuring not to lose any material during both grinding and stirring. After each sample was physically mixed, the total sample was reweighed to ensure negligible to no loss occurred prior to melt quenching the sample. Melt quenching each sample involved the fabrication of borosilicate vacuum sealable glass ampules with the following dimensions: Total length of 5 inches; flared stem length of 4 inches with an I.D. of 8mm; sample housing length of 1inch with an I.D. of 22mm. The sample housing portion of the ampule was blown with a flat bottom to ensure binary mixtures evenly coated the bottom of the ampule. A 6x6 inch VWR weigh paper was then rolled up into a straw and then inserted into the stem of the glass ampule allowing for efficient transfer of sample into the ampule without residual loss that would occur due to static interactions during transfer. The below diagram depicts the vacuum sealable glass ampule design:

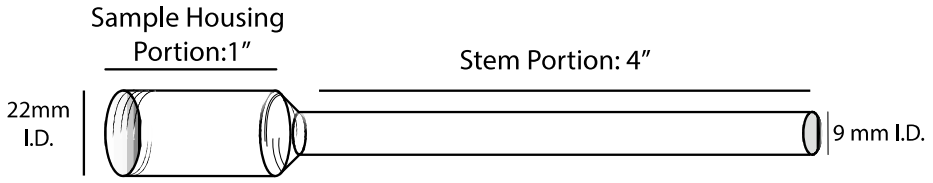

Figure 9: Schematic displaying the dimensions of fabricated flame sealable glass ampules utilized to melt quench ASDs under vacuum conditions to avoid undesired oxidation or degradation during the sample processing.

Once samples were loaded into a glass ampule, they were flame sealed at the ampule stem. The sealed ampules were placed in a Vulcan 3-550 model furnace set at 150˚C and allowed to sit for 10 minutes to allow for thorough melting of the entire sample. Upon removal of, the ampules were immediately submerged in an ice bath until complete solidification of the sample occurred. The hot stick method was applied to open each ampule ensuring no

contamination would occur from borosilicate glass particles. All samples were stored in a desiccator filled with drierite under vacuum pressure at all times unless utilized.

Solution State ^{1}H-NMR Analysis:

Solution state NMR (^{1}H-NMR) was conducted on each sample to determine that the targeted weight % of each sample was achieved. Each proton experiment was conducted on an automated Bruker Ascend 400 magnet utilizing D-chloroform ($CDCl_3$), referenced to 7.24 ppm, as the sample solvent. An ^{1}H 30˚ pulse was used corresponding to an acquisition time of 4.17 s, a sweep width of 9.6 kHz, 32 scans taken with a 10 μs pulse for each experiment, and a recycle delay of 5 s. Samples were further analyzed if observed weight % compositions calculated from relative quantitative measurements differed no more than 3% from the target weight %.

Polarized Light Microscopy:

An Olympus MVX10 Macroview microscope equipped with an MV PLAPO 1X objective lens and two WHSZ20X-H/12.5 eyepieces was utilized to process polarized light microscopy images at 50x magnification. An Olympus SZX-PO polarizing filter was used in conjunction with an Olympus U-AN T2 analyzer slide set 90˚ to the polarizing filter. An Olympus SC100 camera was used to capture images and processed with cellSans Standard 1.7.1 software package. Scrapings from all six samples were placed into VWR glass petri dish and photographed initially with unpolarized light and then under polarized light at 0˚, 45˚, and 90˚ rotated in a clockwise direction to determine any presence of birefringence.

After confirmation of the samples showing no birefringence, they were then further analyzed using solid state NMR.

Differential Scanning Calorimetry:

Differential scanning calorimetry investigation was conducted utilizing a TA instruments DSC2500 calorimeter. Thermodynamic transitions for each of the ASD binary mixtures were analyzed by preparing each sample in clean hermetically sealed Tzero aluminum pans. The average sample weight ranged from 2-10 mg. Indium was chosen to as a reference for all calorimetric investigations, prepared in seperate hermetically sealed pan. Each ASD binary mixture was heated and cooled in the temperature range of -20˚C to 200˚C at rates of 10˚C/minute during heat ramp, and then cooled at rates of 10˚C/minute, 5˚C/minute, and 1˚C/minute. The resulting thermograms were then plotted as a function of heat flow in (W/g) against temperature in (˚C). TA instruments Trio software was utilized to calculate the T_g of each sample from the thermograms by measuring the half height at midpoint temperature. The T_g acquired from each ASD binary samples was then plotted against CBD wt% composition and compared to theoretical calculations derived from the Fox model or the Gordon-Taylor model to assess the accuracy of the results. Equations 2, 3, and 4 were utilized to determine theoretical T_g calculations:

Solid State NMR:

All solid-state NMR spectra were collected using a Varian VNMRS 400 MHz wide-bore spectrometer with a 1.6 mm Transmission Tuning Tube (T3) HXY magic angle spinning (MAS) probe. The downfield methylene peak of adamantane at 38.48 ppm was used as an

external reference.[34] Calibration powers consisting of a 1.25 μs ^{1}H 90˚ pulse power and a 2.5 μs ^{13}C 90˚ pulse power were utilized corresponding to 200.00 kHz and 100.00 kHz respectively for all experiments. The $^{1}H \rightarrow {}^{13}C$ cross-polarization (CP) MAS NMR spectrum of each amorphous solid dispersion composed of CBD and/or PVP was collected at a MAS speed (ω_r) of 35 kHz. The pulse sequence for $^{1}H \rightarrow {}^{13}C$ CP was set with a 2.5 μs ^{13}C pulse corresponding to 100.00 kHz for Hartmann-Hahn (HH) matching conditions. The +1 spinning sideband (ssb) in the HH profile was chosen to match the $^{1}H \rightarrow {}^{13}C$ CP condition which corresponded to 135 kHz. Cross polarization was carried out with a 1.5 ms 2.5 % ramp on the ^{1}H power during the contact time pulse. The ^{1}H decoupling power with a RF field strength of 200.00 kHz was used for all acquisitions. $^{1}H \rightarrow {}^{13}C$ CP MAS spectra were collected using 512 complex points and a recycle delay of 3 s, 8192 transients, and 512 complex points. $^{1}H \rightarrow {}^{13}C$ CP MAS T_1 arrays were collected using 512 complex points along with a recycle delay of 16 s, and 1024 transients. For $^{1}H \rightarrow {}^{13}C$ CP MAS $T_{1\rho}$ array collection, 512 complex points and a recycle delay of 8 s was used when scanning 1024 transients. A ^{1}H spin-lock pulse of 100 kHz RF field strength was applied immediately following an initial 1.25 μs ^{1}H pulse for $T_{1\rho}$ array collection, followed by cross polarization to carbon for detection.

By measuring ^{1}H T_1 and $T_{1\rho}$ relaxation through the lens of ^{13}C nuclei, the proton behavior pertaining each component in the binary mixture could be deciphered. ^{1}H T_1 relaxation constants were obtained using the inversion recovery experiment through ^{13}C observation. The resulting FT spectra from each binary composition provided distinguishable peaks pertaining to each component allowing for the peaks of interest to be integrated and then

plotted against recovery delay times. The integrated values were fitted to equation 5 using a house made R script:

The ^{1}H $T_{1\rho}$ relaxation constants were obtained from measuring the spin-lock duration time of 1 ms after an initial 90˚ pulse to which the resulting FT spectra of each binary composition provided distinguishable peaks pertaining to each component allowing for peak integration to be plotted against recovery delay times. The integrated values were fitted to equation 6 using the same R script:

$$M = M_o - 2M_o\, e^{(-\tau / T1)} \quad (9)$$

$$M = M_o\, e^{(-\tau / T1\rho)} \quad (10)$$

Results and Discussion

Solution State NMR:

The ^{1}H NMR spectra seen in Figure 10 and Figure 11 along with the assignments for each of the peaks. The concentration of CBD in $CDCl_3$ was 4.2 mM while the concentration of PVP in $CDCl_3$ was 1.3 mM. By running a ^{1}H NMR analysis of the two components individually, identification of peaks from both components unaffected by any signal overlap could be evaluated for further quantitative NMR measurements. After evaluating each spectrum, the cis 9 singlet in the CBD spectra found at 4.56 ppm and the broad multiplet in the PVP spectra found at 3.25 ppm were chosen for further quantitative analysis.

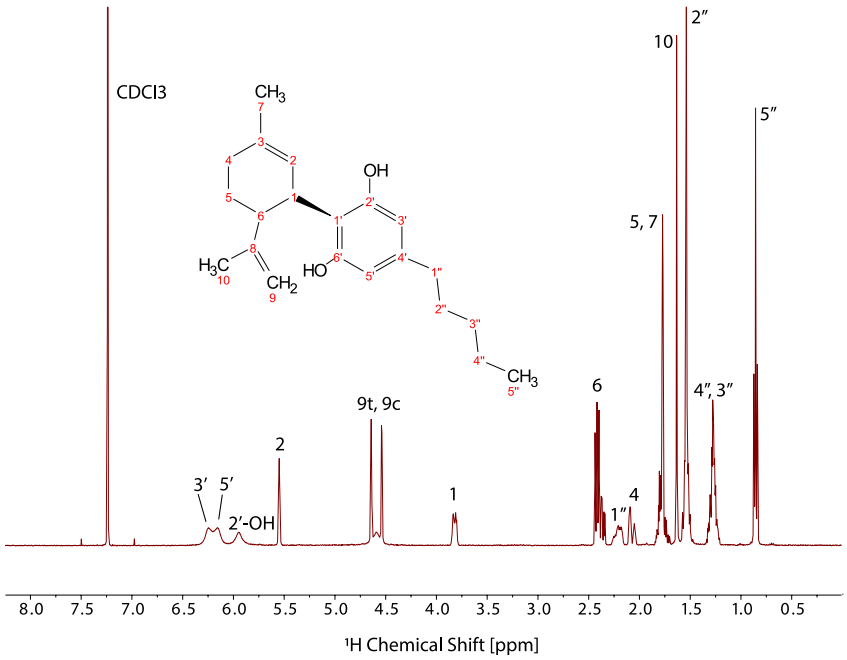

Figure 10: ^{1}H -NMR spectra for CBD in $CDCl_3$. The singlet at 4.5 ppm was utilized to determine quantitative wt% measurements of CBD and PVP for each ASD binary mixture.

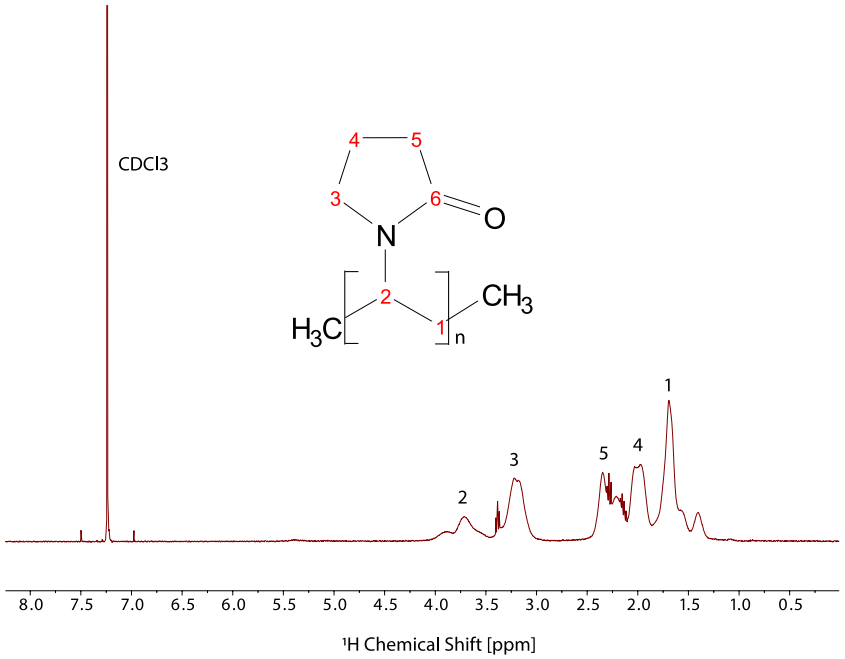

Figure 11: ^{1}H -NMR spectra PVP in CDCl3. The broad multiplet at 3.5 ppm was utilized to determine quantitative wt% measurements of CBD and PVP for each ASD binary mixture.

Table 1 and Figure 11 both correspond to the relative quantitative analysis of each CBD:PVP amorphous solid dispersion binary mixture. Table 1 describes the target wt%, observed wt%, and wt% difference for each binary mixture based on CBD wt% composition. Figure 11 illustrates an array of ^{1}H NMR spectra for each ASD binary mixture dissolved in $CDCl_3$ as well as both components individually ranging from 2.8 – 6.4 ppm. As described previously, the singlet at 4.56 ppm respective of the CBD vinyl protons and the broad multiplet at 3.2 ppm respective of PVP aliphatic protons were utilized to perform a relative quantitative analysis. The observed wt% of each ASD binary mixture prepared differed no more than 3% from the target wt%. As such, each sample was further analyzed via light polarized microscopy and solid-state NMR methods to evaluate sample phase and miscibility.

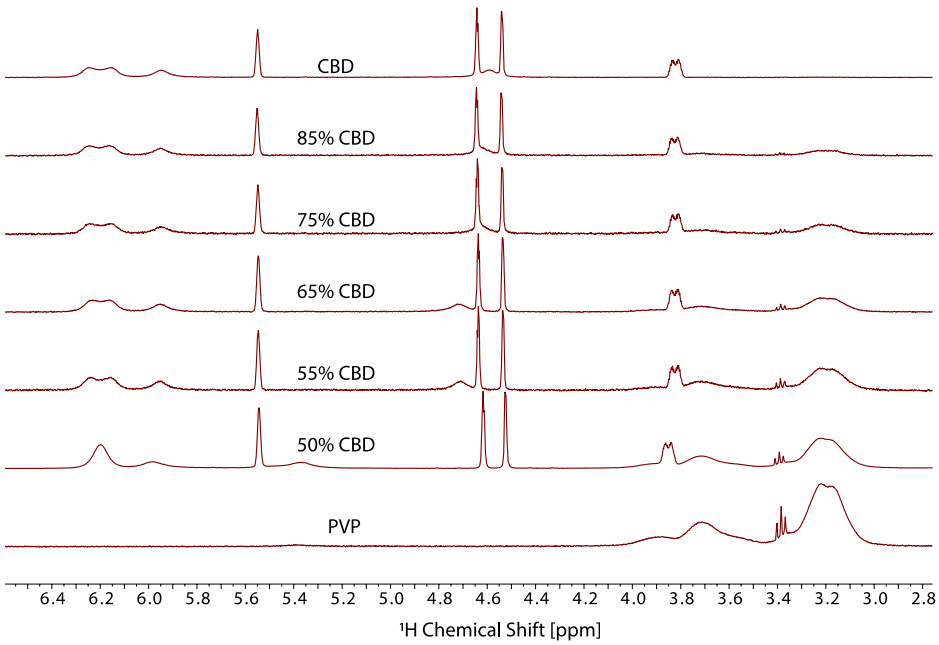

Figure 12: ^{1}H solution-state NMR spectra for a series of CBD:PVP amorphous solid dispersions dissolved in $CDCl_3$. The spectra were collected with a long recycle delay to ensure full relaxation. Careful integration of peaks associated with CBD and PVP allowed for the quantitative measurement of the CBD:PVP wt% ratios for each sample.

Table 1: Targeted and observed ratios for melt-quenched CBD:PVP binary mixtures. Ratios of the final melt-quenched ASDs were observed by careful integration of quantitative NMR spectra

CBD Target wt%:	50.0%	55.0%	65.0%	75.0%	85.0%
CBD Observed wt%:	48.5%	56.7%	65.9%	74.9%	83.1%
Difference in wt%:	3.0%	3.0%	1.4%	0.1%	2.2%

Polarized Light Microscopy:

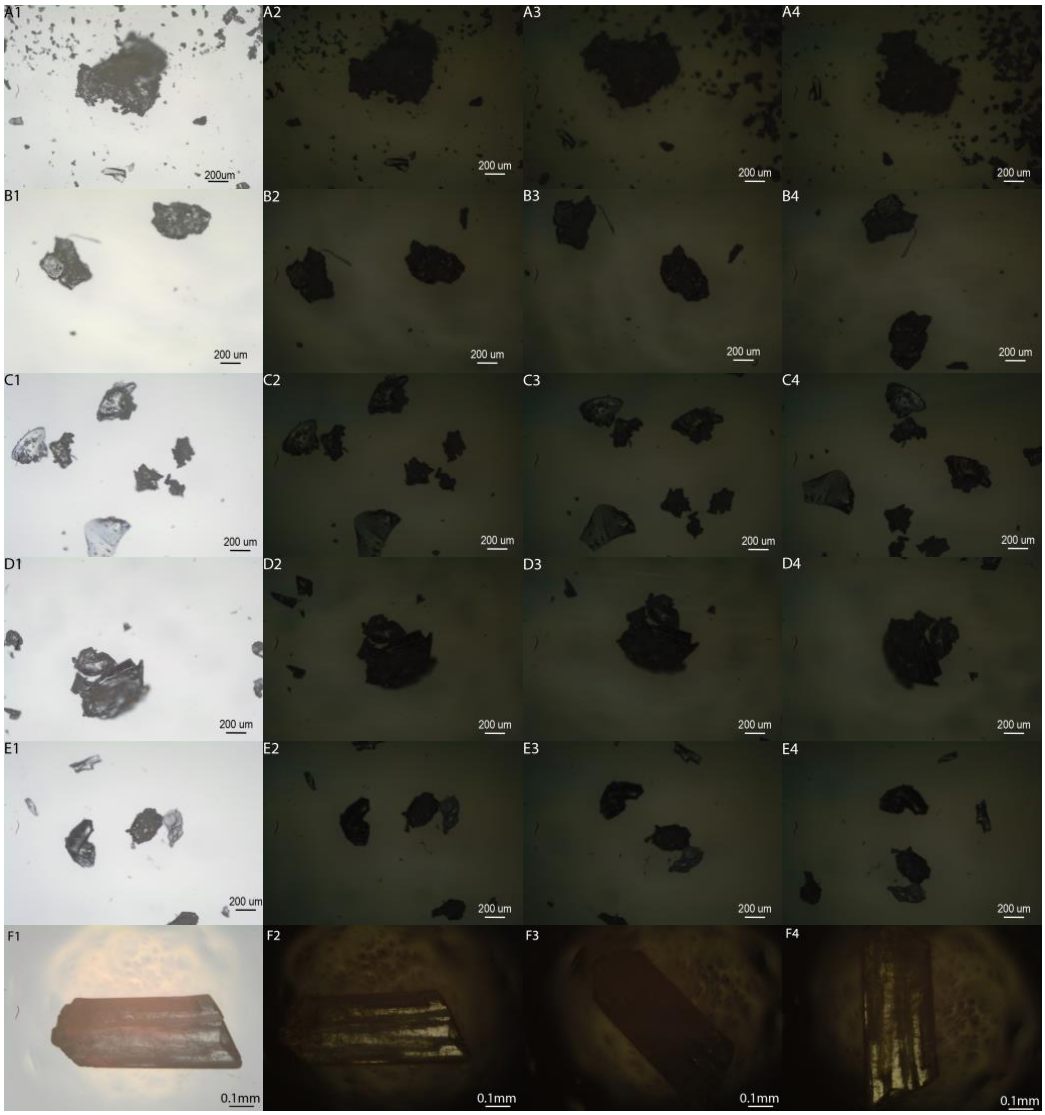

Figure 13: Polarized light microscopy images of CBD:PVP binary amorphous solid dispersion mixtures at wt% **A)** CBD 50% **B)** CBD 55% **C)** CBD 65% **D)** CBD 75% and **E)** CBD 85%. A pure CBD Crystal is shown as a standard at 12.6X magnification in row **F)**. Birefringence is observed at 0˚ and 90˚ rotations. Numbers associated with lettering indicate **1)** unpolarized image, **2)** polarized image at 0˚ rotation, **3)** polarized image at 45˚clockwise rotation, **4)** polarized image at 90˚clockwise rotation. A qualitative analysis of birefringence was conducted indicating that the samples are amorphous.

Each of the ASD binary mixtures prepared were qualitatively analyzed via light polarized microscopy to determine the detection of any birefringence. Any birefringence detected in the sample material would suggest phase separation of the two components and thus indicate the recrystallization of the API. Samples were analyzed via light polarized microscopy immediately after confirmation of wt% composition. As seen in Figure 13, glass shards from each binary mixture were imaged under unpolarized conditions, and then under polarized conditions at 0˚, 45˚, and 90˚ clockwise rotations to determine if any recrystallization had occurred. The polarized images from each binary mixture provided no indication of birefringence and thus were concluded to have held a stable glass phase.

Differential Scanning Calorimetry:

The array of thermograms found in Figure 14 display the glass transition temperatures corresponding to each CBD:PVP ASD binary mixture. A single intermediate T_g was identified for each mixture and recorded. Thermogram B representing binary mixture CBD 50% (w/w) held a T_g at 94.62˚C; Thermogram C representing binary mixture CBD 55% (w/w) held a T_g at 66.32˚C; Thermogram D representing binary mixture CBD 65% (w/w) held a T_g at 54.54˚C; Thermogram E representing binary mixture CBD 75% (w/w) held a T_g at 38.23˚C; and finally Thermogram F representing binary mixture CBD 85% (w/w) held a T_g at 22.85˚C. These values were plotted against wt% composition of CBD to determine how well they fit the Fox-model, Gordon-Taylor-model, and the Kwei model seen in Figure 14. A single intermediate T_g can be observed in each thermogram indicating that each ASD binary mixture is homogenous in domain size of ~ 20 – 30 nm. Unfortunately, during the initial heating process, it is speculated that PVP decomposition

occurred as temperatures approached ~180˚C. The minima resulting from the decomposition peaks were integrated for all samples with no more than ~3.0% decomposition observed and therefore any resulting deviation in T_g values obtained was considered negligible. It should also be noted that the presence of water was detected in these samples as seen in the broad peaks following the T_g points for each sample. As PVP is characterized as being very hydroscopic, water contamination becomes a prevalent issue in the generation of the ASDs.

Figure 15 displays the predicted intermediate T_g's for the five ASD binary mixtures. It was concluded that the predicted T_g values based on the Fox model and the Gordon-Taylor model were far lower than that of the experimental intermediate T_g's. As such the Kwei model was utilized to accurately portray theoretical binary mixture T_g's to which when the parameter q was set to 156, the fitting resembled the observed pattern resulting from the experimental T_g's. This is indicative of large excess energy associated with the stabilization of each mixture and it can be speculated that the hydrogen bonding interactions occurring between the hydroxyl groups of CBD and the carbonyl groups of the repeating PVP monomers are responsible for such a large q value.

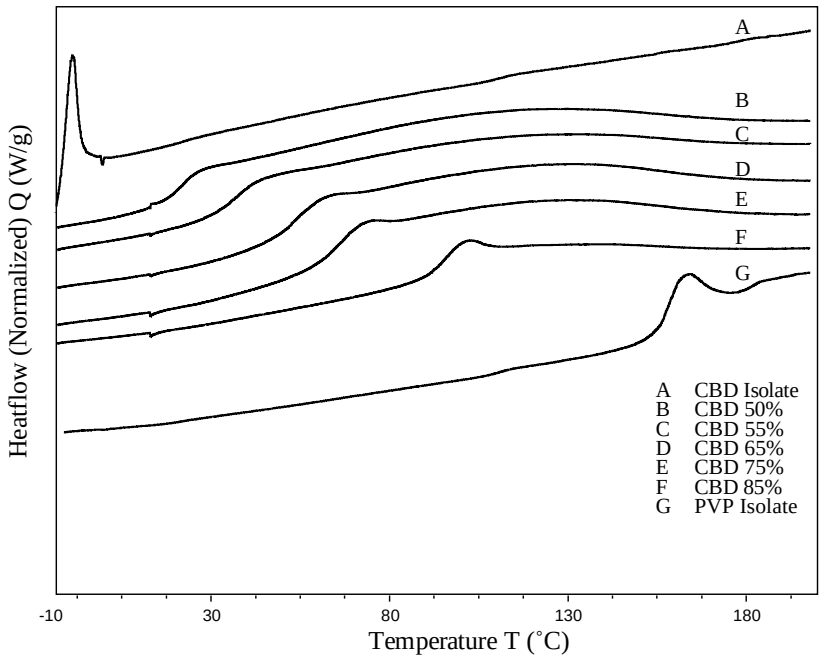

Figure 14: An array of thermograms collected for each ASD binary mixture composed of CBD:PVP. Each sample is represented by wt% composition of CBD. The intermediate T_g of each mixture allows for further wt% content evaluation.

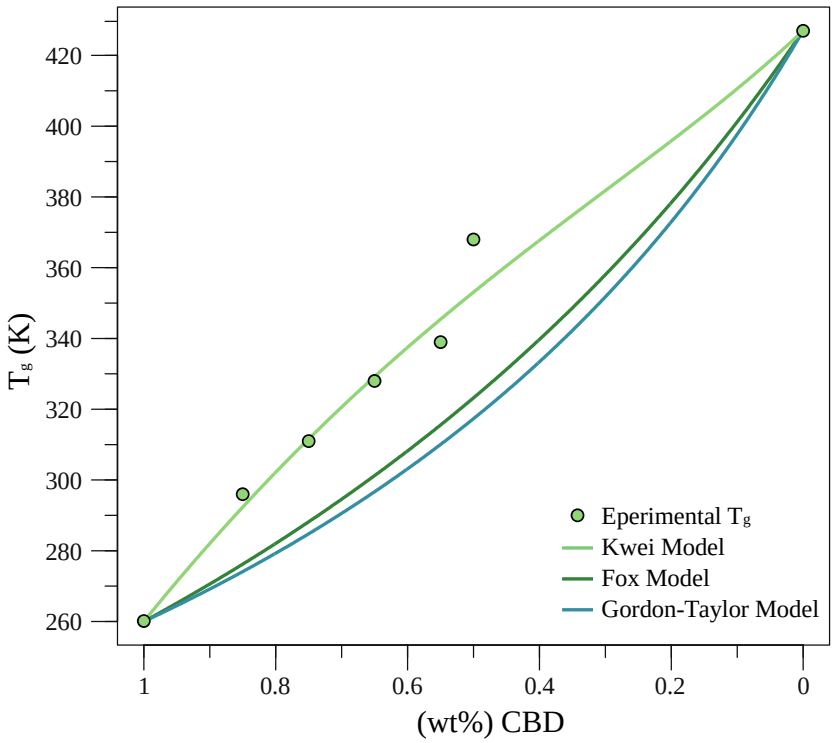

Figure 15: Experimental T_g temperatures in Kelvin plotted against the wt% composition of the five ASD binary mixtures. The teal line represents the Gordon-Taylor model, the dark green line represents the Fox model, and the light green represents the Kwei model. The models were utilized to calculate theoretical T_g temperatures of CBD:PVP ASD binary mixtures in 5% increments based on CBD composition.

Solid State NMR:

^{13}C SSNMR spectra of CBD:PVP amorphous solid dispersions as well as crystalline CBD are shown in Figure 11. The broad peaks observed in each binary mixture are characteristic of amorphous solids. The sharp peaks observed in the crystalline CBD spectra provide a strong contrast in comparison. A single proton T_1 and $T_{1\rho}$ relaxation time was determined for the pure amorphous PVP samples. The ^{13}C SSNMR spectra of CBD:PVP amorphous solid dispersions provided relaxation times based off peaks unaffected by signal overlap. And while the spectra of amorphous solid dispersions resulting from CBD:PVP mixtures limited the peak selection process, peaks around 177 ppm and 42 ppm were selected to calculate the PVP T_1 and $T_{1\rho}$ constants as the CBD peak interference was avoidable when integrating. For the calculation of CBD T_1 and $T_{1\rho}$ constants, peaks at 157 ppm and 143 ppm were chosen as these peaks were unaffected by PVP signal interference.

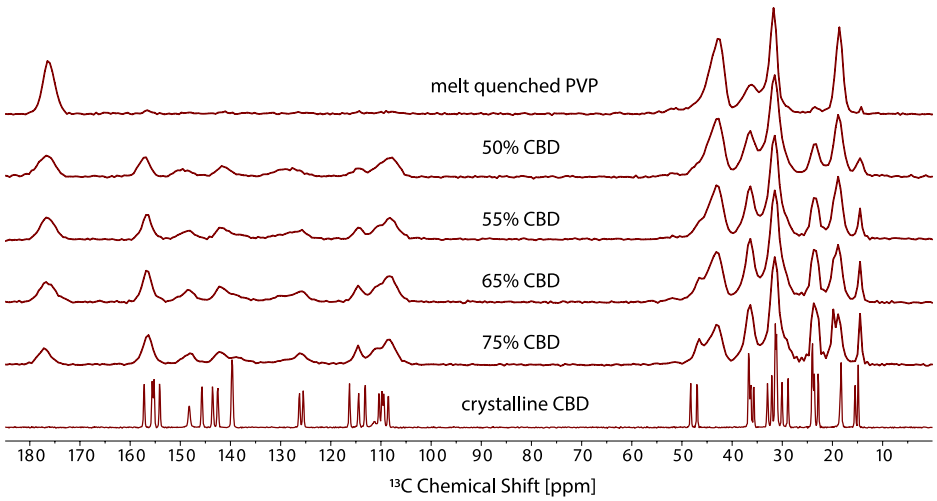

Figure 16: $^{1}H \rightarrow {}^{13}C$ CP-MAS NMR spectra for a series of CBD and PVP amorphous solid dispersions. Crystalline CBD is shown for comparison. The averaged integration of peaks at 177 ppm and 42 ppm for PVP as well as the averaged integration of peaks at 157 ppm and 143 ppm for CBD were utilized to calculate the T_1 and $T_{1\rho}$ time constants.

(A)

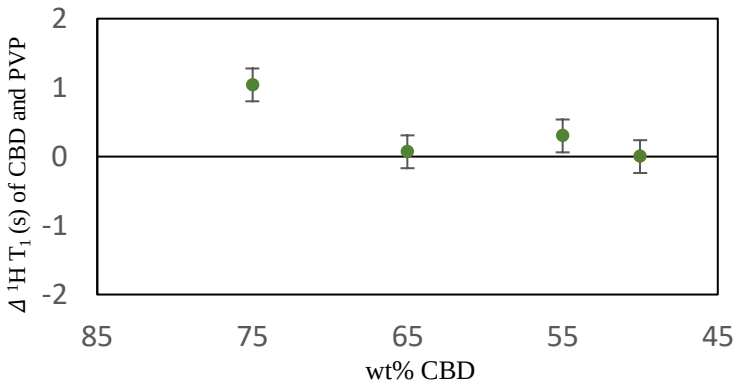

(B)

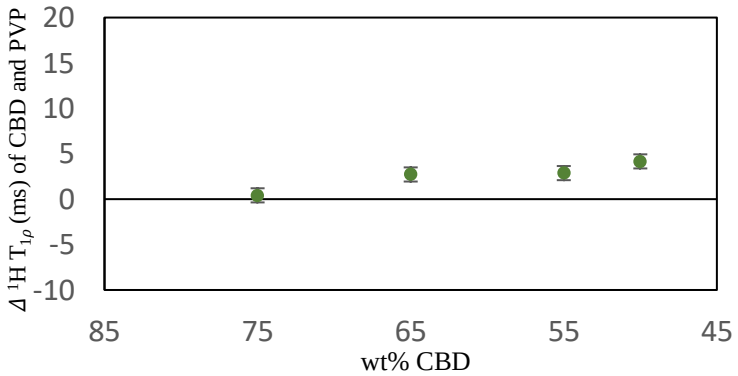

Figure 17: (A) ^{1}H T_1 and (B) ^{1}H $T_{1\rho}$ Time difference comparisons of CBD and PVP amorphous solid dispersions as a function of CBD wt%.

Table 2: ^{1}H T_1 and $T_{1\rho}$ Relaxation Times for CBD:PVP Melt Quenched Amorphous Solid Dispersions

**Values in parenthesis indicate standard errors associated with respective fits.*

		PVP	CBD 50%	CBD 55%	CBD 65%	CBD 75%
Average ^{1}H T_1 (s)	CBD		3.03 (0.38)	3.03 (0.05)	3.09 (0.11)	4.02 (0.43)
	PVP	1.91 (0.04)	3.03 (0.14)	2.73 (0.14)	3.16 (0.09)	2.98 (0.24)
Average ^{1}H $T_{1\rho}$ (ms)	CBD		49.57 (22.4)	12.51 (1.81)	11.92 (1.13)	13.17 (1.69)
	PVP	16.35 (1.18)	45.41 (21.1)	15.38 (2.29)	14.64 (1.56)	13.59 (0.53)

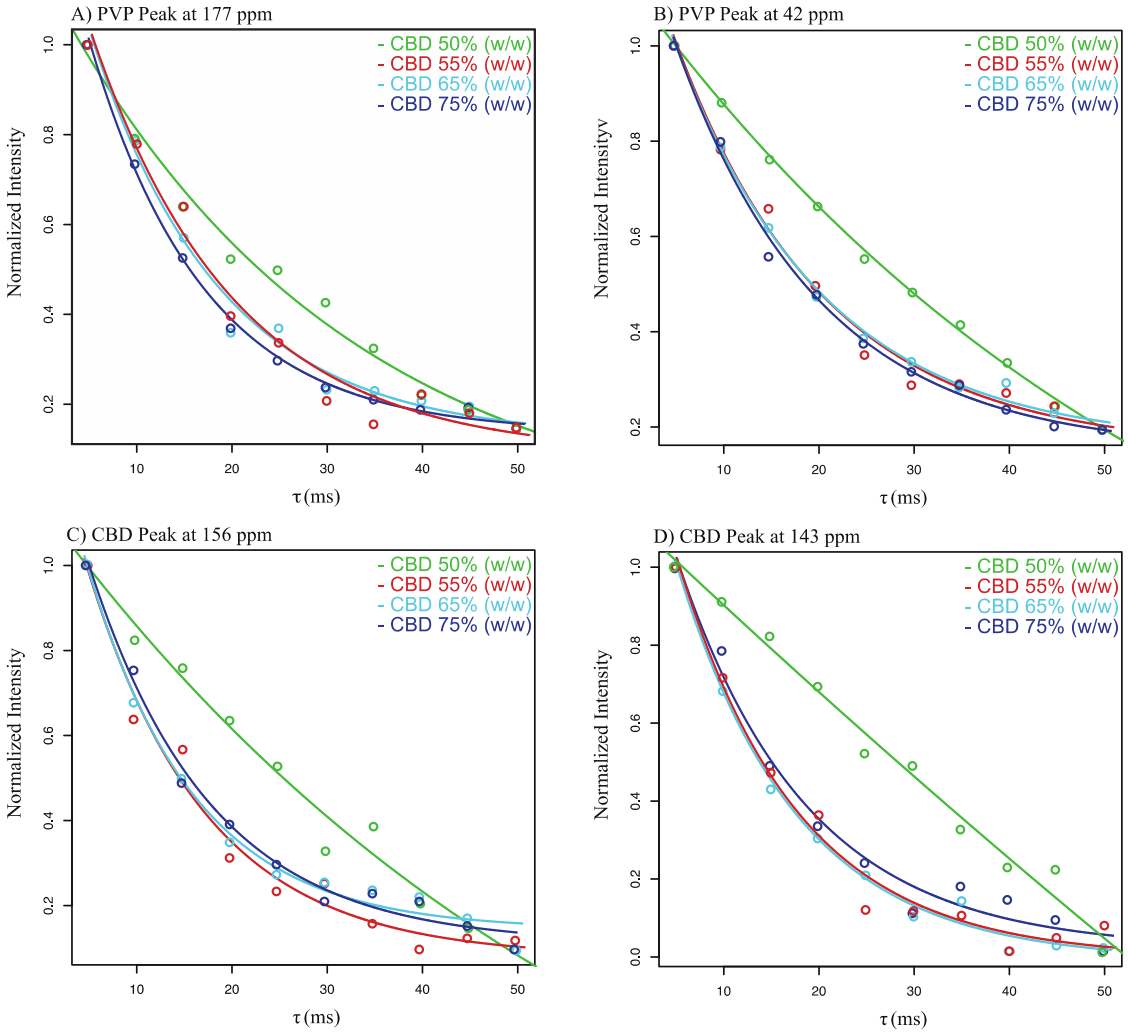

Figure 18: Fittings of $T_{1\rho}$ relaxation delays from ASD binary mixtures. Plots A) and B) represent the fittings gathered from the integration of the peak at 177 ppm and 42 ppm respective of PVP. Plots C) and D) represent the fittings gathered from the integration of peaks at 156 ppm and 143 ppm respective of CBD. The fittings for the ASD binary mixture composed of 50% (w/w) CBD diverges from the characteristic exponential decay behavior and is a result of potential water contamination.

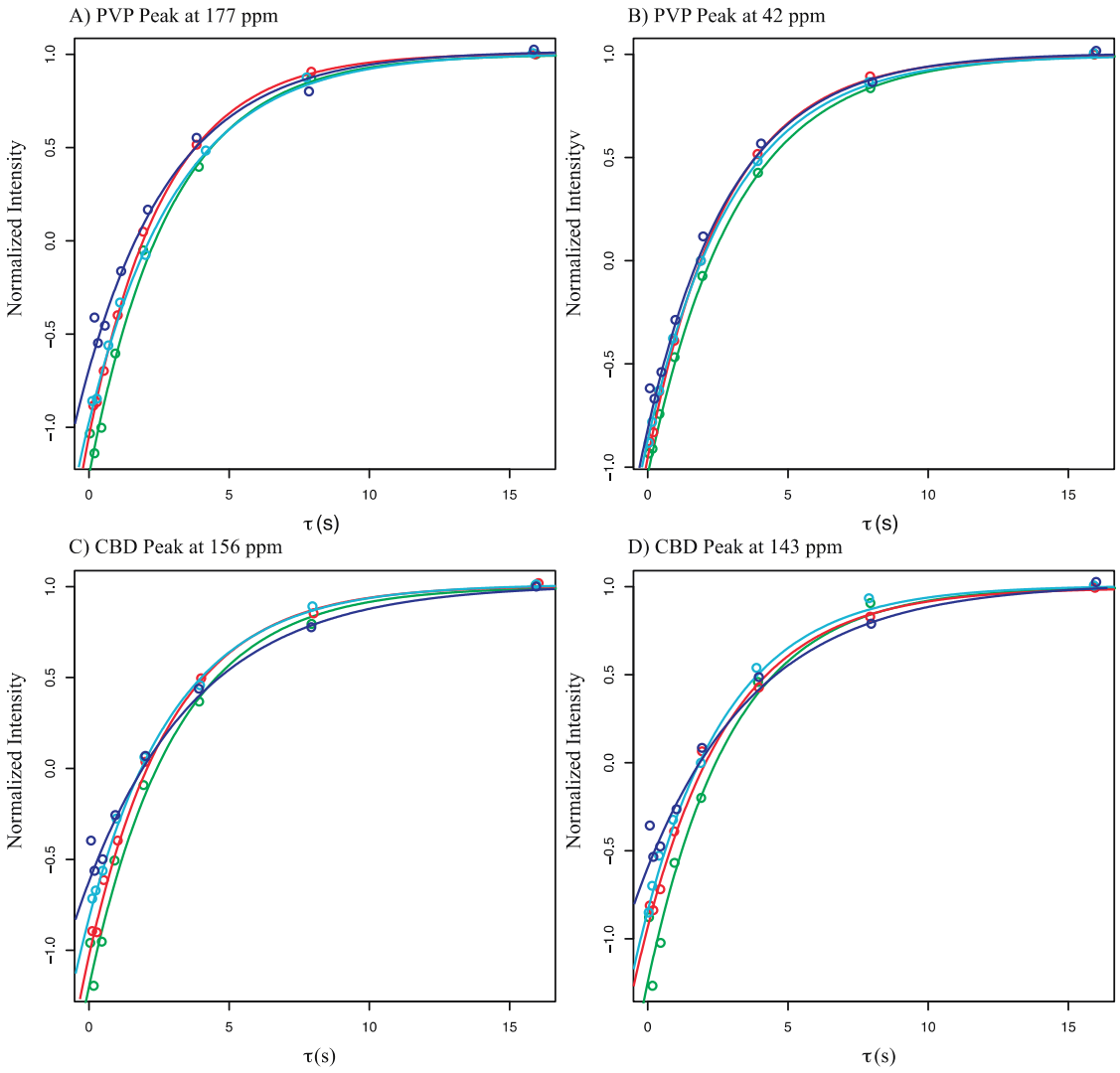

Figure 19: Fittings of T_1 relaxation delays from ASD binary mixtures. Plots A) and B) represent the fittings gathered from the integration of the peak at 177 ppm and 42 ppm respective of PVP. Plots C) and D) represent the fittings gathered from the integration of peaks at 156 ppm and 143 ppm respective of CBD.

Table 2 displays the averaged ^1H T_1 and $T_{1\rho}$ constants obtained from their respective fits. The plottings in Figure 16 and 17 provide the fittings obtained from the $T_{1\rho}$ and T_1 datasets for the 50% - 75% (w/w) CBD ASD samples. Table 2 depicts the series of T_1 and $T_{1\rho}$ constants of pure melt quenched PVP through the melt quenched 75% CBD sample. While the 85% CBD sample was synthesized, and analyzed via solution state NMR and DSC for quantitative assessment as well as qualitatively assessment via PLM, the sample was

characteristic of a "super cooled" liquid with a T_g at approximately room temperature, and thus SSNMR analysis was avoided in fear of causing probe damage. Regardless, the relaxation time constants for the preceding samples were calculated. As seen in Table 2, T_1 time constants varied between CBD and PVP no more than 1.04 s for all samples analyzed, indicating homogeneity in the domain size of 5 – 20 nm. Likewise, the comparison of $T_{1\rho}$ time constants of CBD and PVP showed the largest difference measuring 4.16 ms thus indicating homogeneity in domain sizes smaller than 2 – 5 nm. Figures 18(A) and18(B) provide the comparison of T_1 and $T_{1\rho}$ constant differentials between CBD and PVP as a function of CBD wt% composition. The findings show no obvious trend indicating that these compositions can be concluded as good glass forming ASD binary mixtures up to the limits of 75% (w/w) CBD composition.

In the case of CBD where the T_g of the API is found below room temperature, polyvinylpyrrolidone with an average molecular weight of ~29,000 g/mol was chosen as an ideal polymer to synthesize stable amorphous solid dispersions. The upper limits in terms of wt% composition for each ASD binary mixture created were investigated via polarized light microscopy, differential scanning calorimetry, solution state nuclear magnetic resonance spectroscopy and solid state nuclear magnetic resonance spectroscopy. The above methods of analysis allowed for both qualitative and quantitative analysis and phase assessment of each ASD binary mixture to which homogeneity of each sample was investigated at domain sizes ranging from ~2 – 50 nm. It was concluded that ASD binary mixtures of CBD and PVP in domain ranges of 2 -5 nm were considered homogenous in the glass phase for compositions containing 75% (w/w) CBD, while compositions beyond

that were concluded homogenous at the range of 20 – 30 nm in the super cooled liquid phase.

Conclusion

The pharmacokinetics involved in bioavailability enhancement are critical aspects to evaluate in drug design, especially when an oral therapeutic is the means of administration. It is generally accepted that the phase of an API can greatly alter factors in drug absorption, distribution, and metabolism, as well as excretion. Low energy states associated with crystalline APIs attributed with a discrete molecular lattice have been documented many times to show poor rates of absorption compared to that of an API in the amorphous phase. However, while an API rendered into an amorphous solid dispersion provides improved bioavailability, stability and therefore shelf life of the API becomes a sacrifice in design. This work demonstrates a classical approach to such an obstacle which calls for the intimate mixing of an API and polymer at the molecular level resulting in glass phase stabilization above room temperature. Additionally, the above research conducted shows one of the first attempts at applying a legitimate pharmaceutical approach with respect to drug design utilizing cannabinoids as an API. However, further investigation into this binary system based on humidity, pressure, and time laps is warranted. Additionally, the level of solubility and bioavailability gained from these ASD binary mixtures should be investigated. Finally, similar investigations should be approached with other closely related cannabinoids as the research on the hundreds of cannabinoids already isolated from C. *sativa* is rapidly progressing every day.

Bibliography

(1) Donvito, G.; Nass, S. R.; Wilkerson, J. L.; Curry, Z. A.; Schurman, L. D.; Kinsey, S. G.; Lichtman, A. H. The Endogenous Cannabinoid System: A Budding Source of Targets for Treating Inflammatory and Neuropathic Pain. *Neuropsychopharmacology* **2018**, *43* (1), 52–79. https://doi.org/10.1038/npp.2017.204.

(2) Abuhasira, R.; Schleider, L. B. L.; Mechoulam, R.; Novack, V. Epidemiological Characteristics, Safety and Efficacy of Medical Cannabis in the Elderly. *Eur. J. Intern. Med.* **2018**, *49* (January), 44–50. https://doi.org/10.1016/j.ejim.2018.01.019.

(3) Naftali, T.; Lev, L. B.; Yablekovitz, D.; Half, E.; Konikoff, F. M. Treatment of Crohn's Disease with Cannabis: An Observational Study. *Isr. Med. Assoc. J.* **2011**, *13* (8), 455–458.

(4) Thaler, A.; Arad, S.; Schleider, L. B. L.; Knaani, J.; Taichman, T.; Giladi, N.; Gurevich, T. Single Center Experience with Medical Cannabis in Gilles de La Tourette Syndrome. *Park. Relat. Disord.* **2018**, No. September, 0–1. https://doi.org/10.1016/j.parkreldis.2018.10.004.

(5) Bar-Lev Schleider, L.; Mechoulam, R.; Lederman, V.; Hilou, M.; Lencovsky, O.; Betzalel, O.; Shbiro, L.; Novack, V. Prospective Analysis of Safety and Efficacy of Medical Cannabis in Large Unselected Population of Patients with Cancer. *Eur. J. Intern. Med.* **2018**, *49* (January), 37–43. https://doi.org/10.1016/j.ejim.2018.01.023.

(6) Bar-Lev Schleider, L.; Zerem, A.; Blimkin, L.; Saban, N.; Pelleg, K.; Lerman-Sagie, T.; Linder, I.; Libzon, S.; Levit, L. Medical Cannabis in Children with Complex Motor Disorders. *Eur. J. Paediatr. Neurol.* **2017**, *21*, e219. https://doi.org/10.1016/j.ejpn.2017.04.1132.

(7) Rubio-Araiz, A.; Navarro-Galve, B.; Arévalo-Martín; Guaza, C.; Molina-Holgado, F.; Gómez, O.; García-Ovejero, D.; Molina-Holgado, E. CB 2 Cannabinoid Receptors as an Emerging Target for Demyelinating Diseases: From Neuroimmune Interactions to Cell Replacement Strategies . *Br. J. Pharmacol.* **2007**, *153* (2), 216–225. https://doi.org/10.1038/sj.bjp.0707466.

(8) Mackie, H.-C. L. K. HHS Public Access. **2016**, *79* (7), 516–525. https://doi.org/10.1016/j.biopsych.2015.07.028.An.

(9) Burstein, S. Cannabidiol (CBD) and Its Analogs: A Review of Their Effects on Inflammation. *Bioorganic Med. Chem.* **2015**, *23* (7), 1377–1385. https://doi.org/10.1016/j.bmc.2015.01.059.

(10) Dhopeshwarkar, A.; Mackie, K. CB2 Cannabinoid Receptors as a Therapeutic Target--What Does the Future Hold? *Mol. Pharmacol.* **2014**, *86* (4), 430–437. https://doi.org/10.1124/mol.114.094649.

(11) Graham, P. L. *An Introduction to Medicinal Chemistry*, Sixth.; Oxford University Press: Oxford, 2017.

(12) Newman, A.; Munson, E. Characterizing Miscibility in Amorphous Solid Dispersions. *Am. Pharm. Rev.* **2012**, *15* (3), 1–6.

(13) elikbilek, M.; Erin, A.; Ayd, S. Crystallization Kinetics of Amorphous Materials. *Adv. Cryst. Process.* **2012**. https://doi.org/10.5772/35347.

(14) Ediger, M. D.; Angell, C. A.; Nagel, S. R. Supercooled Liquids and Glasses. *J. Phys. Chem.* **1996**, *100* (31), 13200–13212. https://doi.org/10.1021/jp953538d.

(15) Kapko, V.; Zhao, Z.; Matyushov, D. V.; Austen Angell, C. "Ideal Glassformers" vs "Ideal Glasses": Studies of Crystal-Free Routes to the Glassy State by "Potential Tuning" Molecular Dynamics, and Laboratory Calorimetry. *J. Chem. Phys.* **2013**, *138* (12). https://doi.org/10.1063/1.4794787.

(16) Yuan, X.; Sperger, D.; Munson, E. J. Investigating Miscibility and Molecular Mobility of Nifedipine-PVP Amorphous Solid Dispersions Using Solid-State NMR Spectroscopy. *Mol. Pharm.* **2014**, *11* (1), 329–337. https://doi.org/10.1021/mp400498n.

(17) Masuda, K.; Tabata, S.; Sakata, Y.; Hayase, T.; Yonemochi, E.; Terada, K. Comparison of Molecular Mobility in the Glassy State between Amorphous Indomethacin and Salicin Based on Spin-Lattice Relaxation Times. *Pharm. Res.* **2005**, *22* (5), 797–805. https://doi.org/10.1007/s11095-005-2597-4.

(18) Ditzinger, F.; Scherer, U.; Schönenberger, M.; Holm, R.; Kuentz, M. Modified Polymer Matrix in Pharmaceutical Hot Melt Extrusion by Molecular Interactions with a Carboxylic Coformer. *Mol. Pharm.* **2019**, *16* (1), 141–150. https://doi.org/10.1021/acs.molpharmaceut.8b00920.

(19) Qian, F.; Huang, J.; Zhu, Q.; Haddadin, R.; Gawel, J.; Garmise, R.; Hussain, M. Is a Distinctive Single Tg a Reliable Indicator for the Homogeneity of Amorphous Solid Dispersion? *Int. J. Pharm.* **2010**, *395* (1–2), 232–235. https://doi.org/10.1016/j.ijpharm.2010.05.033.

(20) Nidhi, K.; Indrajeet, S.; Khushboo, M.; Gauri, K.; Sen, D. J. Microstructural Imaging of Early Gel Layer Formation in HPMC Matrices. *J. Pharm. Sci.* **2006**, *95* (10), 2145–2157. https://doi.org/10.1002/jps.

(21) McBrierty, V. J.; Douglass, D. C.; Kwei, T. K. Compatibility in Blends of Poly(Methyl Methacrylate) and Poly(Styrene-Co-Acrylonitrile). 2. An NMR Study. *Macromolecules* **1978**, *11* (6), 1265–1267. https://doi.org/10.1021/ma60066a038.

(22) Basics of Polarizing Microscopy. *Olympus* **2010**, 28. https://doi.org/10.1002/cyto.990200308.

(23) MAS Spinning Guide v. 1.0. 1–31.

(24) Lodge, T. P.; Wood, E. R.; Haley, J. C. Two Calorimetric Glass Transitions Do Not Necessarily Indicate Immiscibility: The Case of PEO/PMMA. *J. Polym. Sci. Part B Polym. Phys.* **2006**, *44* (4), 756–763. https://doi.org/10.1002/polb.20735.

(25) Manuscript, A. Binary Blends of Sugars and Salts. **2015**, *68* (1), 155–158. https://doi.org/10.1016/j.cryobiol.2013.12.005.Application.

(26) Lin, A. A.; Kwei, T. K.; Reiser, A. On the Physical Meaning of the Kwei Equation for the Glass Transition Temperature of Polymer Blends. *Macromolecules* **1989**, *22* (10), 4112–4119. https://doi.org/10.1021/ma00200a052.

(27) Pinal, R. Entropy of Mixing and the Glass Transition of Amorphous Mixtures. *Entropy* **2008**, *10* (3), 207–223. https://doi.org/10.3390/entropy-e10030207.

(28) Schneider, H. A.; Rieger, J.; Penzel, E. The Glass Transition Temperature of Random Copolymers: 2. Extension of the Gordon - Taylor Equation for Asymmetric Tgvs Composition Curves. *Polymer (Guildf).* **1997**, *38* (6), 1323–1337. https://doi.org/10.1016/S0032-3861(96)00652-0.

(29) Nmr, H. Ig Origins of Solid-State NMR.

(30) Berendt, R. T.; Sperger, D. M.; Munson, E. J.; Isbester, P. K. Solid-State NMR Spectroscopy in Pharmaceutical Research and Analysis. *TrAC - Trends Anal. Chem.* **2006**, *25* (10), 977–984. https://doi.org/10.1016/j.trac.2006.07.006.

(31) Corporate, G. E. Spin Lattice Relaxation in Lithium-Sodium. **1979**, 5–9.

(32) BRONDEAU, J.; CANET, D.; WERBELOW, L.; CHAUMETTE, H.; GRANDCLAUDE, D. Rotating-Frame Spin—Lattice Relaxation Measurements (T 1ρ) with Weak Spin-Locking Fields in the Presence of Homonuclear Dipolar Coupling . *Mol. Phys.* **2004**, *101* (12), 1919–1926. https://doi.org/10.1080/0026897031000112460.

(33) Aso, Y.; Yoshioka, S.; Miyazaki, T.; Kawanishi, T.; Tanaka, K.; Kitamura, S.; Takakura, A.; Hayashi, T.; Muranushi, N. Miscibility of Nifedipine and Hydrophilic Polymers as Measured by (1)H-NMR Spin-Lattice Relaxation. *Chem. Pharm. Bull. (Tokyo).* **2007**, *55* (8), 1227–1231. https://doi.org/10.1248/cpb.55.1227.

(34) Morcombe, C. R.; Zilm, K. W. Chemical Shift Referencing in MAS Solid State NMR. *J. Magn. Reson.* **2003**, *162* (2), 479–486. https://doi.org/10.1016/S1090-7807(03)00082-X.